Available online at www.sciencedirect.com
SCIENCE DIRECT®
International Journal of Solids and Structures 42 (2005) 727–750
INTERNATIONAL JOURNAL OF SOLIDS and STRUCTURES
www.elsevier.com/locate/ijsolstr

# Structure of weak shock waves in 2-D layered material systems

Liren Tsai, Vikas Prakash *

*Department of Mechanical and Aerospace Engineering, Case Western Reserve University, 10900 Euclid Avenue, Cleveland, OH 44106-7222, USA*

Received 15 April 2004
Available online 6 August 2004

**Abstract**

Shock waves in homogeneous materials in the absence of phase transitions are understood to have a one-wave structure. However, upon loading of a layered heterogeneous material system a two-wave structure is obtained—a leading shock front followed by a complex pattern that varies with time. This dual shock-wave pattern can be attributed to material architecture through which the shock wave propagates, i.e. the impedance (and geometric) mismatch present at various length scales, and nonlinearities arising from material inelasticity and failure.

The objective of the present paper is to provide a better understanding of the role of material architecture in determining the structure of weak shock waves in 2-D layered material systems. Normal plate-impact experiments are conducted on 2-D layered material targets to obtain both the precursor decay and the late-time dispersion. The particle velocity at the free surface of the target plate is measured by using a multi-beam VALYN VISAR. In order to understand the effects of layer thickness and the distance of wave propagation on elastic precursor decay and late-time dispersion several different targets with various layer and target thicknesses are employed. Moreover, in order to understand the effects of material inelasticity both elastic–elastic and elastic–viscoelastic bilaminates are utilized.

The results of these experiments are interpreted by using asymptotic techniques to analyze propagation of acceleration waves in 2-D layered material systems. The analysis makes use of the Laplace transform and Floquet theory for ODE's with periodic coefficients [Asymptotic solutions for wave propagation in elastic and viscoelastic bilaminates. In: Developments in Mechanics, Proceedings of the 14th Mid-Eastern Mechanics Conference, vol. 26, no. 8, pp. 399–417]. Both wave-front and late-time solutions for step-pulse loading on layered half-space are compared with the experimental observations. The results of the study indicate that the structure of acceleration waves is strongly influenced by impedance mismatch of the layers constituting the laminates, density of interfaces, distance of wave propagation, and the material inelasticity.


*Keywords:* 2-D layered materials; Heterogeneous materials; Elastic–elastic bilaminates; Elastic–viscoelastic bilaminates; Wave propagation; Impedance mismatch; Density of interfaces; Asymptotic methods; Precursor decay; Late-time dispersion; Plate-impact experiments

* Corresponding author. Tel.: +1 216 368 6440; fax: +1 216 368 3007.
*E-mail address:* prakash@mae.cwru.edu (V. Prakash).

0020-7683/$ - see front matter © 2004 Elsevier Ltd. All rights reserved.
doi:10.1016/j.ijsolstr.2004.06.030

## 1. Introduction

The understanding of behavior of materials under dynamic loading conditions is vital to many areas of both civil and military applications. Better understanding of dynamic response has important practical implications connected with impact and blast mitigation, design of lightweight armor, as well as optimal design of other engineered structures with potential danger of shock loading. Currently, a number of material systems ranging from metal, ceramics, and polymers in both monolithic and composite forms are being used to achieve a combination of characteristics to meet the desired goals. Some of the recent examples highlighting the success of these systems include woven composites and functionally graded materials. Also, composite materials with organic matrices reinforced by synthetic or ceramic fibers either individually or in combination with monolithic ceramic layers are being used to achieve light weight and enhanced ballistic impact resistance (Sherby et al., 1990; Betheney et al., 1998; Vaidya et al., 1999; Fink, 2000).

A large body of knowledge currently exists in the literature on the propagation of acceleration waves and finite amplitude shock waves in heterogeneous materials. For such systems, scattering, dispersion and attenuation play a critical role in determining the thermo-mechanical response of the media. These phenomena can be attributed to a number of nonlinearities arising from the wave characteristics, loading conditions, and material heterogeneity (measured at various spatial scales ranging from nanometers to a few millimeters). The nonlinear effects due to material heterogeneity can be ascribed to impedance (and geometric) mismatch present at various length scales, apart from material nonlinearities arising from material inelasticity effects, void nucleation and growth, and delamination.

Even though some progress has been made in understanding the propagation of acceleration waves in heterogeneous material systems, the phenomenon of material and geometric dispersion in these materials continues to be poorly understood. Shock waves in the absence of phase transitions are understood to have a one-wave structure in most homogeneous materials. However, upon loading of a bi-laminate, a two-wave structure is obtained—a leading shock front followed by a complex pattern that varies with time. This complex pattern is generated by a continuous interaction of compression and rarefaction waves due to the presence of inter-laminar interfaces. Expressions for pressure and particle-velocity, based on the consideration of head-wave interaction with interfaces in linear elastic bilaminates under weak shock wave loading have been obtained by Laptev and Trishin (1976). It was found that the attenuation of shock pressure and particle velocity is primarily determined by the ratio of acoustic impedance of the layers, and by the size of the periodic structure of the bilaminates (cell size). Smaller the cell size, the greater is the number of interfaces that interact with the propagating stress waves, and higher is the attenuation and dispersion. Analytical studies of wave dispersion relations for an infinite train of time-harmonic acceleration waves propagating in layered material systems have been conducted in a variety of elastic composites. Sun et al. (1968) studied the case of waves in elastic bilaminates (i.e. composites consisting of alternating plane layers of different linear elastic materials) propagating in directions parallel or perpendicular to the laminates. These exact dispersion relations have been compared by Hegemier (1972) to those obtained from various approximate theories. For viscoelastic bilaminates the understanding of dispersion relations is less complete. Stern et al. (1970) have considered wave propagation in a direction parallel to the laminates for alternating layers of elastic and viscoelastic materials. They simplified the analysis by neglecting the transverse displacement in the viscoelastic layers and the variation of the longitudinal displacement across the thickness of the elastic layers. Clifton (1972) considered the exact theory of time-harmonic waves propagating in the direction of the normal to the laminates for general linear viscoelastic bilaminates. The dispersion relations obtained were similar to those obtained by Sve (1971) for the closely related case of thermo-elastic waves in laminates. Transient solutions for the case of step loading applied uniformly over the surface of a half space consisting of alternating plane layers of elastic materials have been obtained by Peck and Gurtman (1969)

and by Sve (1972) who considered, respectively, waves propagating parallel and perpendicular to the layers. In both these cases late-time asymptotic solutions were obtained which show the dispersive character of the main part of the wave. Sve (1972) also considered, in an approximate way, the late-time solution for viscoelastic bilaminates in which the waves are propagating in the direction perpendicular to the laminates.

To date, only a limited number of experiments have been carried out that concern the finite amplitude wave propagation in composite materials for the loading stress in the intermediate regime. Barker et al. (1974) performed experiments on periodic laminates and found that below certain critical input amplitude, the stress wave amplitude decayed exponentially with distance and formed a structured shock wave above the critical amplitude. Lundergan and Drumheller (1971) and Oved et al. (1978) also conducted limited shock wave experiments on layered stacks, which showed resonance phenomena due to layering. Nesterenko et al. (1983, 1984) observed an anomaly in the precursor decay for the case of propagation of strong shock waves in periodic bilaminates with a relatively small cell size. They noted that for bilaminates with a relatively small cell size the jump in particle velocity at the wave front is essentially higher than one obtained with the larger cell size at the same distance of propagation. Similar observations were made for Ti–Al layered material systems under strong shock wave loading (Benson and Nesterenko, 2001). Comparison of the experimental results and computer simulations indicated that this effect is primarily due to the interactions of the secondary compression waves with the leading shock front. At early times, these secondary compression waves trail the shock front. However, with increasing distance of propagation these waves catch-up and eventually overtake the leading shock-wave front from behind. This increase in wave speed is facilitated by the propagation of the trailing secondary waves in a previously compressed material state. More recently Zhuang (2002) have conducted normal plate-impact experiments on layered stacks of polycarbonate and either glass, stainless steel or aluminum systems to investigate dispersion versus dissipation characteristics due to heterogeneity of the layered material system during propagation of strong shock waves. They also reviewed existing models for propagation of shock waves and proposed new scaling laws for shock viscosity of heterogeneous layered solids.

In view of the scientific and technological importance of heterogeneous materials in shock related applications and our current incomplete state of understanding of their performance under impact loading conditions, an integrated experimental–analytical program of research is being conducted at CWRU. The focus of the proposed research is to better understand wave scattering and dispersion at material interfaces and the role of material inelasticity in determining the structure of shocks during shock compression in heterogeneous material systems. In the present paper asymptotic techniques have been employed to analyze propagation of acceleration waves in 2-D layered material systems. In order to understand elucidate the effects of layer thickness and impedance mismatch on elastic precursor decay and late-time dispersion, wave propagation in elastic bilaminates is analyzed. Moreover, wave propagation in 2-D elastic–viscoelastic bilaminates is analyzed to understand the effects of material inelasticity on both the wave-front and late-time solutions. The use of bilaminates provides a more tractable geometry from both analytical and experimental considerations. The analysis makes use of the Laplace transform and of the Floquet theory for ordinary differential equations with periodic coefficients (Chen and Clifton, 1974). Both wave-front and late-time solutions for step-pulse loading on layered half-space are presented. In addition, normal plate-impact experiments are conducted to obtain both precursor decay and the late-time dispersion. The elastic–elastic bilaminates are impacted by an elastic flyer plate using the 82.5 mm single-stage gas–gun facility at CWRU. The free-surface particle velocity at the rear of the target plate is measured by using a multi-beam VALYN VISAR (Velocity Interferometer System for Any Reflector) and compared with the predictions of the analytical solutions. These comparisons are used to understand the effects of layer thickness, impedance mismatch, and material inelasticity on precursor decay and late-time dispersion.

## 2. Analytical analysis

### 2.1. Wave propagation in elastic–viscoelastic bilaminates

Consider bilaminates consisting of elastic and viscoelastic layers of uniform thickness and infinite lateral extent. The elastic layers occupy odd numbered layers, i.e. $n = 1,3,5,\ldots$, and the viscoelastic layers occupy even numbered layers, i.e. $n = 2,4,6,\ldots$ Consider the individual layers to be homogeneous and isotropic and the layer thickness of both constituents to be the same, i.e. $L_1 = L_2 = 0.5d$, where $L_1$ and $L_2$ are the thickness of the elastic and viscoelastic layers, respectively, and $d$ is the total thickness of a typical bilaminate.

Let the laminates be subjected to a time dependent normal stress loading which is applied uniformly over the plane $x = 0$ (see Fig. 1). Under these conditions longitudinal wave of one-dimensional strain propagate in the direction normal to the laminates. We consider the case in which the applied loading has a step function time dependence, i.e. $\sigma = -\sigma_0 \mathrm{H}(t)$, and seek asymptotic solutions for the wave at the wave-front and the waveform at late times.

For infinitesimal deformation longitudinal waves propagating in the $x$-direction are governed by the balance of linear momentum and continuity. For the elastic layers these equations can be written as

$$\rho_1 \frac{\partial u_1}{\partial t}(x,t) - \frac{\partial \sigma_1}{\partial x}(x,t) = 0 \quad \text{and} \quad \frac{\partial \varepsilon_1}{\partial t}(x,t) = \frac{\partial u_1}{\partial x}(x,t). \tag{1}$$

For viscoelastic layers the balance of linear momentum and the continuity equations can be written as

$$\rho_2 \frac{\partial u_2}{\partial t}(x,t) - \frac{\partial \sigma_2}{\partial x}(x,t) = 0 \quad \text{and} \quad \frac{\partial \varepsilon_2}{\partial t}(x,t) = \frac{\partial u_2}{\partial x}(x,t). \tag{2}$$

The constitutive equations for elastic and viscoelastic layers can be expressed as

$$\sigma_1(x,t) = E\varepsilon_1(x,t) \quad \text{and} \quad \sigma_2(x,t) = \int_{-\infty}^{t} G(t-\tau)\,\mathrm{d}\varepsilon_2, \quad \text{respectively.} \tag{3}$$

In Eqs. (1)–(3), $\sigma_1$ and $\sigma_2$ are the longitudinal components of the stress in the elastic and viscoelastic layers, $u_1$ and $u_2$ are the longitudinal components of the particle velocities in the elastic and viscoelastic layers, $\rho_1$ and $\rho_2$ are the mass density of the elastic and the viscoelastic layers, $\varepsilon_1$ and $\varepsilon_2$ are the longitudinal compo-

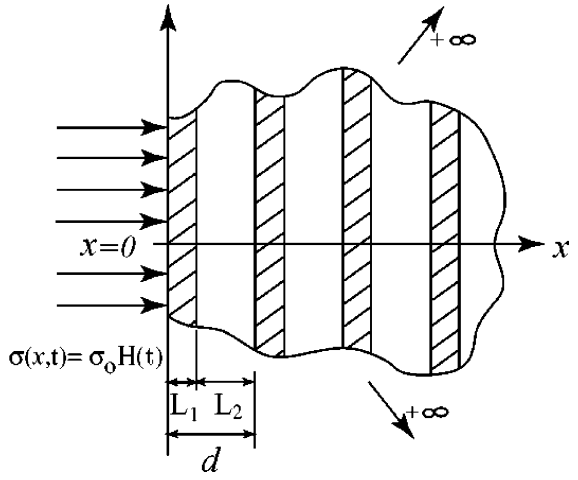


Fig. 1. Schematic of the laminate used in the analytical analysis.

nents of the strain in the elastic and viscoelastic layers, and $E$ and $G(t)$ represent the elastic and the viscoelastic modulus, respectively.

The relaxation function for the viscoelastic material behavior is assumed to be described by an exponential function of the type

$$G(t) = [G(0) - G(\infty)]\mathrm{e}^{-t/\tau} + G(\infty), \tag{4}$$

where, $G(0)$ denotes the "glassy" modulus at $t = 0$, $G(\infty)$ denotes the "rubbery" modulus at $t = \infty$, and $\tau$ denotes the characteristic relaxation time.

We seek solution to Eqs. (1)–(3) which satisfy zero stress and zero particle-velocity initial conditions, and boundary conditions given by $\sigma(0,t) = -\sigma_0 H(t)$. Solutions to such problems are obtained most conveniently by means of Laplace Transform methods in which the Laplace transform, $\hat{f}(x,s)$, of a function $f(x,t)$ is defined by

$$\hat{f}(x,s) = \int_0^\infty f(x,t)\mathrm{e}^{-st}\,\mathrm{d}t. \tag{5}$$

Application of the Laplace transform to Eqs. (1)–(3) yields a system of four algebraic equations in the transformed plane. For a fixed $s$, these equations represent ordinary differential equations in which the coefficients are periodic functions of $x$ with period $d = L_1 + L_2$. These equations contain four complex constants associated with the solution for the longitudinal component of stress. Two conditions on the four complex constants are obtained by requiring that the particle velocity and stress be continuous across the interface between the two adjacent layers comprising the bilaminate. The remaining conditions are obtained by the application of Floquet theory for periodic structures (Chen and Clifton, 1974). According to Floquet's theory, for such differential equations the solution at an arbitrary position $x$ is related to the solution at $x-d$ by

$$\hat{w}(x,s) = \mathrm{e}^{\mu(s)d}\hat{w}(x-d,s), \tag{6}$$

where $\hat{w}(x,s)$ represents the solution vector for the particle velocity and stress and $\mu(s)$ is a characteristic parameter to be determined.

The characteristic parameter $\mu(s)$ in Eq. (6) can be obtained by solving the transcendental equation

$$\cosh\mu(s)d = \cosh\alpha_1(s)l_1\cosh\alpha_2(s)l_2 + \frac{1}{2}\left(\frac{\rho_1\alpha_1(s)}{\rho_2\alpha_2(s)} + \frac{\rho_2\alpha_2(s)}{\rho_1\alpha_1(s)}\right)\sinh\alpha_1(s)l_1\sinh\alpha_2(s)l_2, \tag{7}$$

where

$$\alpha_1(s) = \sqrt{\frac{s^2\rho_1}{E}} \quad \text{and} \quad \alpha_2(s) = \sqrt{\frac{s\rho_2}{\widehat{G}(s)}}. \tag{8}$$

Note that if $\mu$ is a solution of Eq. (7), then $-\mu$ is also a solution. By considering wave propagation in the direction of increasing $x$, we can restrict our attention to roots for which $\mathrm{Re}\mu(s) \leqslant 0$, so that the solution remains bounded as $x \to \infty$. This requirement uniquely determines $\mu$, except for added integer multiples of $2\pi i$ which do not affect the solution.

## 3. Solution at wave-front: elastic precursor decay

Let the longitudinal wave-fronts propagate with speeds $c_1$ and $c_2$ in the elastic and the viscoelastic layers, respectively. An average wave speed for the longitudinal wave-fronts can be defined as

$$c_{\text{wave}} = \frac{d}{(l_1/c_1 + l_2/c_2)}. \tag{9}$$

At the arrival of the longitudinal wave at $x = x_n$, where $x_n = (n/2)d$ is the distance from $x = 0$ to the interface between the $n$th and the $(n+1)$th layers, the stress is given by

$$\sigma(x_n, x_n^+/c_{\text{wave}}) = -\sigma_0 \left\{ \exp\left[\frac{l_2 G'(0)}{2c_2 G(0)}\right] \right\}^{n/2} \theta^{-n/2}, \tag{10}$$

where

$$\theta = \frac{1}{2} + \frac{1}{4}\left(\frac{\rho_2 c_2}{\rho_1 c_1} + \frac{\rho_1 c_1}{\rho_2 c_2}\right). \tag{11}$$

For the case of elastic–elastic bilaminates the argument of the exponential function is zero and the RHS of Eq. (10) can be interpreted as an average transmission coefficient for propagation of an elastic wave through a cell of length $d$. The attenuation of the amplitude at the wave-front is the decay primarily due to successive elastic wave reflections. For the case of elastic–viscoelastic bilaminates the argument of the exponential function gives rise to additional attenuation due to material inelasticity. The rate of decrease in stress is often so rapid that the stress at the wave front can become negligibly small at remote positions.

Fig. 2 shows the magnitude of the elastic precursor as a function of number of layers and the impedance mismatch. The $x$-axis represents the impedance mismatch between the layers while the $y$-axis represents the layer number, i.e. the distance of wave propagation. A strong decay in the elastic precursor is observed with an increase in the number of layers and/or the increase in impedance mismatch.

Fig. 3 shows the effect of viscoelasticity on the elastic precursor decay after wave propagation through 10 layers. The stress at the wave front is normalized by the amplitude of the corresponding elastic precursor for the case of elastic–elastic bilaminates. The $x$-axis represents the ratio of the time taken for the longitudinal wave to travel the thickness of a viscoelastic layer to the relaxation time constant for the material. It is to be noted that when the relaxation time is large and/or the viscoelastic layer thickness, i.e. $L_2$, is small, the effect of material inelasticity on elastic precursor decay is small. Also, when the ratio between the instantaneous modulus and the rubbery modulus, i.e. $\gamma^2 = G(0)/G(\infty)$, is close to one the effect of material inelasticity on the elastic precursor decay is negligible.

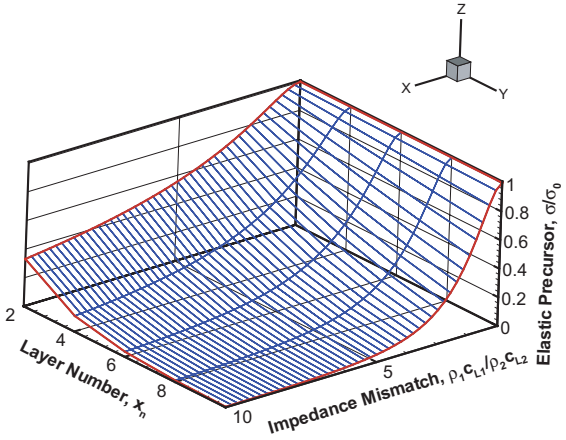


Fig. 2. Effect of material mismatch and the number of layers on the elastic precursor decay for elastic–elastic bilaminates.

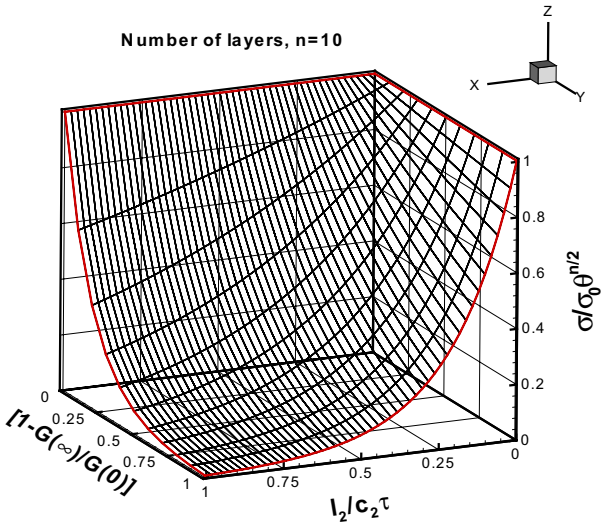


Fig. 3. Effect of material inelasticity on the elastic precursor decay. The stress at the wave front ($y$-axis) is normalized by the amplitude of the elastic precursor for the case of elastic–elastic bilaminates.

## 4. Late-time asymptotic solution

At sufficiently late times after the arrival of the wave front, the stress at a remote position is expected to reach a level $\sigma_0$, which corresponds to the applied stress boundary condition at $x = 0$. The transition from the low-amplitude stress at the wave front to this equilibrium state at late-times can be characterized by obtaining the late-time asymptotic solution to the integral

$$\sigma(x_n, t) = \frac{1}{2\pi i} \int_{\gamma - i\infty}^{\gamma + i\infty} \hat{\sigma}(x_n, s) \mathrm{e}^{st} \, \mathrm{d}s. \tag{12}$$

The integral in Eq. (12) can be evaluated asymptotically for large $t$ by using the method of steepest descent. To this end, it is convenient to introduce the small time scale

$$\delta = t - x_n / c_{\text{lave}} \tag{13}$$

in which $c_{\text{lave}}$ denotes the average wave-speed at which the main parts of the longitudinal disturbance propagates at late time and is given by

$$c_{\text{lave}} = \frac{d}{\left[ \left( \frac{l_1}{c_1} \right)^2 + \left( \frac{l_2}{c_2} \right)^2 + \left( \frac{\rho_1 c_1}{\rho_2 c_2} + \frac{\rho_2 c_2}{\rho_1 c_1} \right) \left( \frac{l_1}{c_1} \right) \left( \frac{l_2}{c_2} \right) \right]^{1/2}}. \tag{14}$$

It should be noted that $c_{\text{lave}}$ is equivalent to defining the phase velocity of an infinite train of sinusoidal waves of zero frequency, i.e. the long wavelength limit. It is interesting to note that the speed of longitudinal disturbance at late times depends on the impedance mismatch between the layers. For laminate architectures in which the impedance mismatch is close to one, the late-time dispersion wave and the elastic precursor arrive at a particular location at the same time. However, for laminates in which the impedance mismatch is large, $c_{\text{lave}}$ is considerably less than $c_{\text{wave}}$. This effect is shown graphically in Fig. 4 for a select number of material pairs.

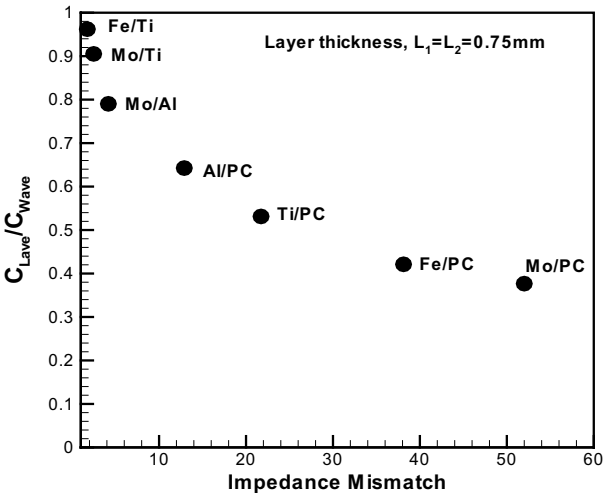


Fig. 4. The effect of impedance mismatch on the average wave speed $c_{lave}$ at which the main parts of the longitudinal disturbance propagate at late times.

Substituting Eq. (13) in Eq. (12), we can obtain an alternate form of the inverse transform, i.e.

$$\sigma(x_n,t)=\frac{\sigma_0}{2\pi i}\int_{\Gamma-i\infty}^{\Gamma+i\infty}\frac{\mathrm{e}^{-\delta g(s)}\,\mathrm{e}^{th(s)}}{s}\,\mathrm{d}s, \tag{15}$$

where

$$g(s)=\mu(s)c_{\mathrm{lave}} \tag{16}$$

and

$$h(s)=\mu(s)c_{\mathrm{lave}}+s. \tag{17}$$

In order to evaluate the integral in Eq. (15) for $t\to\infty$, we employ the method of steepest descent (Achenbach, 1973). In view of this it must be noted that the main contribution to the integral is expected to arise from $s=0$. Expanding $h(s)$ about the saddle point $s=0$ gives

$$g(s)\cong -s+\frac{h''(0)}{2!}s^2+\frac{h'''(0)}{3!}s^3 \tag{18}$$

and

$$h(s)\cong \frac{h''(0)}{2!}s^2+\frac{h'''(0)}{3!}s^3. \tag{19}$$

In Eqs. (18) and (19), $h''(0)$ and $h'''(0)$ are given by

$$h''(0)=\frac{c_{\mathrm{lave}}^2}{d^2}\left(\left[\frac{l_2^2}{c_2^2}\tau(\gamma^2-1)\right]-\frac{l_1l_2}{c_1c_2}\left[\tau(\gamma^2-1)\left(\frac{\rho_1c_1}{\rho_2c_2}\right)\right]\right) \tag{20}$$

and

$$\begin{aligned}h'''(0)=\frac{c_{\mathrm{lave}}^4}{d^4}\frac{l_2(l_2\rho_2+l_1\rho_1)}{4c_1^6\rho_2^3\rho_1^3c_2^6}\Big\{&c_1^2l_1^2l_2\rho_2^3\rho_1(l_2\rho_2-2l_1\rho_1)c_2^4+l_1^3l_2\rho_2^5c_2^6\\&+c_1^6l_2\rho_1^3\big(l_1^2l_2\rho_1^2+3(1+2\gamma^2-3\gamma^4)l_2\rho_2^2\tau^2c_2^2\big)+3(1+2\gamma^2-3\gamma^4)l_1\rho_2\rho_1\tau^2c_2^2\\&+c_1^4l_1\rho_2\rho_1^2c_2^2\big(l_1^2l_2\rho_1^2-12\gamma^2(\gamma^2-1)l_2\rho_2^2\tau^2c_2^2-21\rho_2\rho_1\big(l_2^2+6\gamma^2(\gamma^2-1)\tau^2c_2^2\big)\big)\Big\},\end{aligned} \tag{21}$$

where, as before, $\gamma^2$ is the ratio between the instantaneous modulus and the rubbery modulus.

In view of Eqs. (15)–(19), the integral in Eq. (15) along the path of steepest descent $\Gamma$ can be written as

$$\sigma(x,\delta)=\frac{\sigma_0}{2\pi i}\int_\Gamma \frac{1}{s}\mathrm{e}^{-\left\{\frac{h'''(0)}{3!}s^3+\frac{h''(0)}{2!}s^2-s\right\}\delta+\left\{\frac{h'''(0)}{3!}s^3+\frac{h''(0)}{2!}s^2\right\}t}\,\mathrm{d}s=\frac{\sigma_0}{2\pi i}\int_\Gamma \frac{1}{s}\mathrm{e}^{\delta s+(t-\delta)\frac{h''(0)}{2!}s^2+(t-\delta)\frac{h'''(0)}{3!}s^3}\,\mathrm{d}s. \tag{22}$$

Substituting Eq. (13) into Eq. (22) and applying the transformation

$$s=z\left[\frac{6}{(x_n/c_{\mathrm{lave}})h''(0)}\right]^{1/3}-\frac{h''(0)}{h'''(0)} \tag{23}$$

yields

$$\sigma(x_n,t)=\mathrm{e}^A\frac{\sigma_0}{2\pi i}\int_{\Gamma_z}\frac{\mathrm{e}^{Bz+z^3}}{z}\,\mathrm{d}z. \tag{24}$$

In Eq. (24)

$$A=-(t-x_n/c_{\mathrm{lave}})\frac{h''(0)}{h'''(0)}+\frac{1}{3}\frac{(h''(0))^3}{(h'''(0))^2}(x_n/c_{\mathrm{lave}}) \tag{25}$$

and

$$B=\left[(t-x_n/c_{\mathrm{lave}})-\frac{1}{2}\frac{[h''(0)]^2}{h'''(0)}(x_n/c_{\mathrm{lave}})\right]\left(\frac{6}{h'''(0)(x_n/c_{\mathrm{lave}})}\right)^{1/3}. \tag{26}$$

The path of steepest descent $\Gamma$ approaches $s=0$ along the directions $\arg(s)=-\frac{\pi}{3}$; it is indented to the right around the pole $s=0$ and leaves the origin along the direction $\arg(s)=\frac{\pi}{3}$. The contribution to the integral from the one-third of a circle indentation around the origin is $\sigma_0/3$. Thus, the integral in Eq. (24) along the steepest descent path becomes (Cerrillo, 1950)

$$\sigma(x_n,t)=\mathrm{e}^A\sigma_0\left[\frac{1}{3}+\int_0^B \mathrm{Ah}(B)\,\mathrm{d}B\right], \tag{27}$$

in which $\mathrm{Ah}(B)$ is the Airy Hardy function

$$\mathrm{Ah}(B)=\frac{1}{2\pi i}\int_\Gamma \mathrm{e}^{Bz+z^3}\,\mathrm{d}z. \tag{28}$$

After certain algebraic manipulations it can be shown that Eq. (12) can be expressed as

$$\sigma(x_n,t)=\sigma_0\mathrm{e}^A\left[\frac{1}{3}+\sum_{m=0}^{\infty}\frac{\Gamma\left(\frac{m+1}{3}\right)}{(m+1)!}B^{m+1}\sin\left(\frac{\pi}{3}(m+1)\right)\right], \tag{29}$$

where $\Gamma(m)$ is the gamma function defined as

$$\Gamma(m)=\int_0^\infty t^{m-1}\mathrm{e}^{-t}\,\mathrm{d}t\quad\text{for } m>0. \tag{30}$$

For infinitesimal deformation, solutions for elastic precursor decay and late-time dispersion which satisfy zero stress and particle velocity initial conditions and boundary conditions given by a step loading function in time, are summarized in Fig. 5. Upon impact of the laminate, a two wave structure is obtained. The leading elastic precursor propagates at a speed dictated by the average wave speed in the two constituents given by $c_{\mathrm{wave}}$, while the late-time dispersed front arrives at a speed $c_{\mathrm{lave}}$. The late-time stress wave oscillates about a mean level dictated by the amplitude of the input stress pulse.

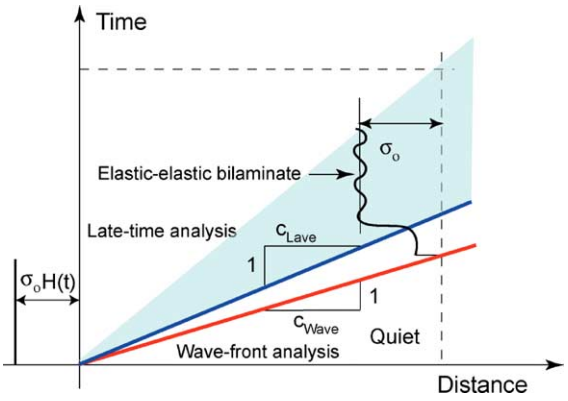


Fig. 5. The two wave structure obtained during impact of a typical elastic bi-laminate.

Next, stress wave profiles obtained from the asymptotic solutions at the wave front and the waveform at late times are presented. These simulations are designed to illustrate the effect of impedance mismatch, distance of wave propagation, layer thickness, i.e. cell size, density of interfaces, and material inealsticity on the amplitude of stress wave at the wave front and the dispersive characteristics of the waveform at late times. The simulations are carried out for elastic–elastic bilaminates comprising Ti–Fe and Mo–Ti material pairs, and elastic–viscoelastic bilaminates comprising Al–PC material pair. The acoustic impedance mismatch for Ti–Fe and Mo–Ti bilaminates is 1.75 and 2.45, respectively. For the Al–PC bilaminates the acoustic impedance mismatch is 8.31. Three different layer thicknesses are evaluated for the Ti–Fe and Mo–Ti laminates: 0.75, 1.5 and 2.25 mm for total laminate thickness of 9 mm. For the Al–PC laminates the simulations are presented for layer thickness of 0.125 mm with total laminate thicknesses of 0.5, 1.0 and 1.5 mm. The relaxation time in Eq. (4) for PC is taken to be $\tau = 2$ μs. The ratio of the instantaneous modulus to the rubbery modulus, i.e. $G(0)/G(\infty)$, is taken to be 1.01. Table 1 gives the physical properties of all the materials used in the simulations.

Figs. 6 and 7 present the predictions of the wave profiles for elastic–elastic bilaminates illustrating the effects of impedance mismatch on the wave front and late-time dispersion wave characteristics. Two different bilaminates are considered: Fe–Ti bilaminates with an impedance mismatch of 1.75 and Mo–Ti bilaminates with an impedance mismatch of 2.48. In each case the thickness of the individual layers is 0.75 mm. The abscissa represents the time after impact while the ordinate represents the theoretical normal stress normalized by the amplitude of the input stress. The stress profiles are shown at a propagation distance of 3, 6, and 9 mm. As discussed earlier, for each laminate a two-wave structure is obtained. A leading wave front (elastic precursor) that propagates at the speed $c_{\text{wave}}$, and a late-time dispersion wave propagating at the speed $c_{\text{lave}}$. For the case of Mo–Ti bilaminates a larger precursor decay as well as a lower frequency of

Table 1
Physical properties of the material layers employed in the simulations

| Layer material | Elastic modulus (GPa) | Density (g/cm$^3$) | Longitudinal wave speed (m/s) | Acoustic impedance (GPa mm/μs) |
|---|---|---|---|---|
| Titanium (Ti) | 120.2 | 4.5 | 6716 | 30.22 |
| Iron (Fe) | 211.4 | 7.87 | 5950 | 46.83 |
| Molybdenum (Mo) | 324.8 | 10.22 | 6250 | 63.88 |
| Aluminum (Al) | 70.6 | 2.7 | 6420 | 17.33 |
| Polycarbonate (PC) | 2.3 | 1.2 | 1832 | 2.20 |

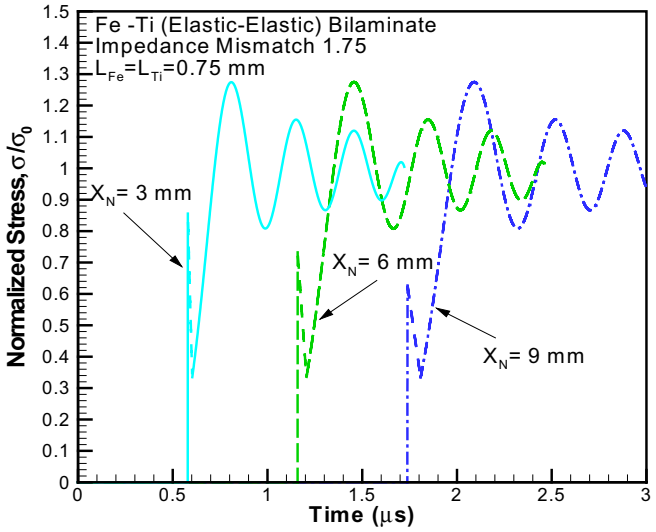


Fig. 6. Effect of distance of propagation on the elastic precursor and late-time dispersion for Fe–Ti laminates.

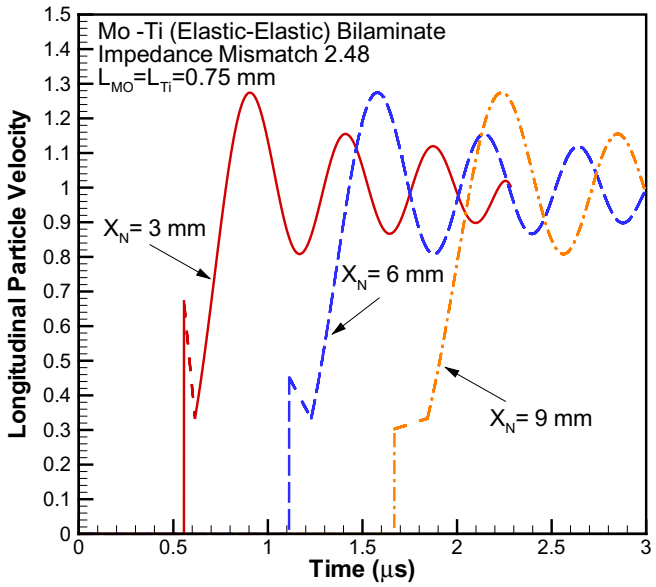


Fig. 7. Effect of distance of propagation on the elastic precursor and late-time dispersion for Mo–Ti laminates.

the late-time dispersive waves is observed. Also, consistent with Eqs. (9) and (14), the time difference between the arrival of the leading wave front and the late-time dispersive wave is much longer in the case of Mo–Ti laminates when compared with the Fe–Ti laminates. It is also interesting to note that in both cases the late-time dispersive waves show steady wave profiles with increasing distance of propagation into the bilaminates.

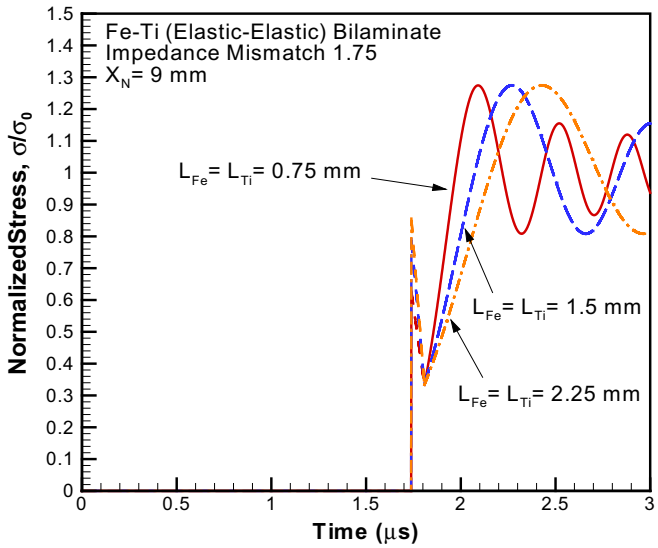


Fig. 8. Effect of layer thickness on the elastic precursor and the late-time dispersion for Fe–Ti laminates.

Fig. 8 shows the effect of the layer thickness on the elastic precursor decay and late-time dispersion during propagation of stress waves in Ti–Fe laminates. Results for three different layer thicknesses are presented: 0.75, 1.5 and 2.25 mm. As expected, the arrival of the elastic precursor at $x_n = 9$ mm occurs at the same time for the three different laminate architectures. However, the laminates with largest layer thickness, i.e. 2.25 mm, shows the smallest elastic precursor decay, while the laminate with the smallest layer thickness, i.e. 0.75 mm, shows the highest precursor decay. The late-time dispersive wave for the smallest layer thickness laminates contain the highest frequency oscillations while the largest layer thickness laminates contain the lowest frequency oscillations. Also, the rise-time associated with the late-time dispersive wave decreases with layer thickness and an increase in the density of interfaces (i.e. number of layers in a given laminate thickness).

Fig. 9 shows the wave-front as well as the late-time solution for the Al–PC laminate for $x_n = 0.5$, 1 and 1.5 mm. The impedance mismatch for the Al–PC material pair is 8.3. The thickness of each Al and PC layer is 0.125 mm. Due to the relatively high impedance mismatch between the Al and PC layers, and also the viscoelasticity associated with PC, a very strong elastic precursor decay is observed; so-much-so that the elastic precursor is reduced to approximately zero as the stress wave propagates only 0.5 mm into the laminate. This is seen more clearly from the insert in Fig. 9, which shows the early parts of the wave profiles for the three thicknesses. Also, it is interesting to observe that the frequency of the oscillations in the late-time dispersive wave solution is much smaller when compared to the lower impedance mismatch Mo–Ti and Ti–Fe material pair laminates.

Fig. 10 compares the late-time dispersion characteristics for several select material pairs with different impedance mismatch laminates. Because of the dependence of $c_{\text{lave}}$ on the impedance mismatch, the dispersion profiles have been shifted in time so as to start at the same point in time. The late-time dispersion profiles can be characterized by the rise time and the frequency of the oscillations contained in the wave profiles. The rise times of the dispersion waves is observed to increase with an increase in impedance mismatch, while the frequency of the oscillations decreases with an increase in the impedance mismatch. Also, the late-time dispersive wave oscillates about the mean level corresponding to the input stress. The maxi-

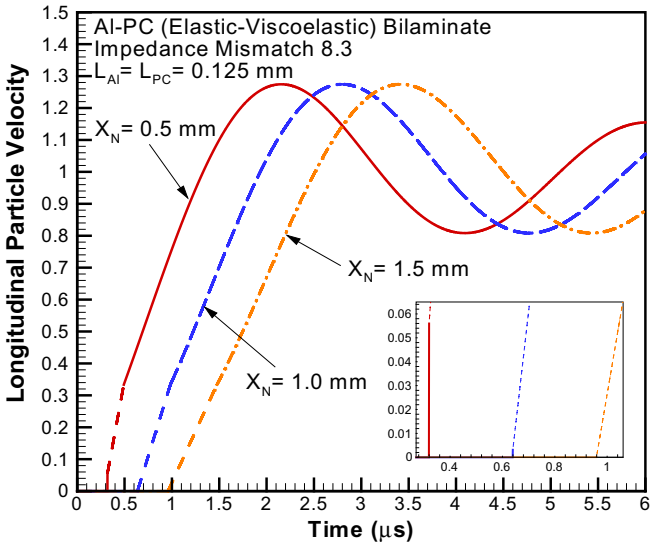


Fig. 9. Wave front and late-time dispersion results for Al–PC bilaminates.

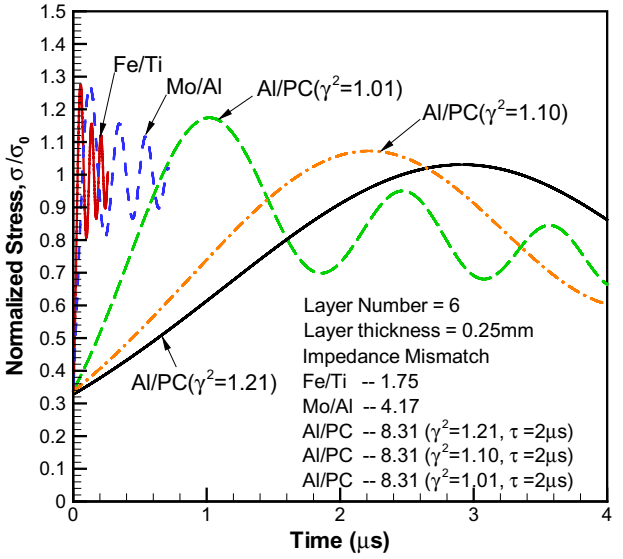


Fig. 10. Characteristics of late-time dispersion for select material pairs with different impedance mismatch.

mum amplitude of the late-time dispersion wave is $\sim 1.3\sigma_0$, and is observed to be independent of the impedance mismatch of the elastic–elastic laminates. Also, it is interesting to note the effect of material inelasticity on the dispersion characteristics of the late-time wave profiles. With an increase in the ratio between the instantaneous modulus to the rubbery modulus the rise time associated with the late time dispersive waves is observed to increase while the frequency of the oscillations decreases.

## 5. Experimental results and discussion

### 5.1. Experimental configuration

The experiments described in this paper are designed to illustrate the effect of impedance mismatch, layer thickness, and material inelasticity on the elastic precursor decay and late-time dispersion characteristics of weak shock waves in 2-D laminates. In view of this, normal plate impact experiments are conducted on laminates comprising alternating Ti–Fe (elastic–elastic) and the Al–PC (elastic–viscoelastic) layers. The experiments are conducted using the 82.5 mm single-stage gas–gun at Case Western Reserve University. The experiments involve the impact of an elastic flyer plate with a target assembly at normal incidence. The target assembly is a sandwich in which the laminate under investigation is confined between two metal plates that remain elastic under impact. Impact takes place on the front target plate; the waves transmitted through the layered specimen are monitored on the free surface of the rear target plate by means of laser interferometer. The measured motion at the free surface of the rear target plate and the known elastic properties of the front and the rear target plates are used to obtain the wave characteristics as the shock wave propagates through the layered specimen.

The schematic of the plate-impact experimental configuration is shown in Fig. 11. A fiberglass projectile carrying the flyer plate is accelerated down the gun barrel by means of compressed nitrogen gas. The rear end of the projectile has sealing O-ring and a plastic (Teflon) key that slides in a key-way inside the gun barrel to prevent any rotation of the projectile. In order to reduce the possibility of an air cushion between the flyer and target plates, impact takes place in a target chamber that has been evacuated to 50 μm of Hg prior to impact. A laser based optical system utilizing a UNIPHASE Helium–Neon 5 mW laser (Model 1125p) and a high frequency photo-diode is used to measure the velocity of the projectile. To ensure the generation of plane waves with wave-front sufficiently parallel to the impact face, the flyer and the target plates are carefully aligned to be parallel to within $2 \times 10^{-5}$ radians by using an optical alignment scheme. The actual tilt between the two plates is measured by recording the times at which four, isolated, voltage-biased pins, that are flush with the surface of the target plate, are shorted to ground. The acceptance level of the experiments is of the order of 0.5 mrad. A VALYN VISAR laser interferometer is used to measure the history of the normal particle velocity at the rear surface of the target plate. A COHERENT VERDI 5 Watt solid-state diode-pumped frequency doubled Nd:$YVO_4$ CW laser with wavelength of 532 nm is used to provide a coherent monochromatic light source.

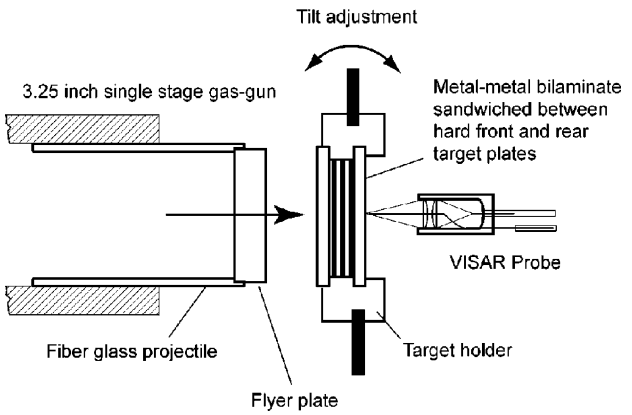


Fig. 11. Schematic of the plate-impact configuration employed in the present investigation. The layered specimen is sandwiched between two hard plates of the target assembly.

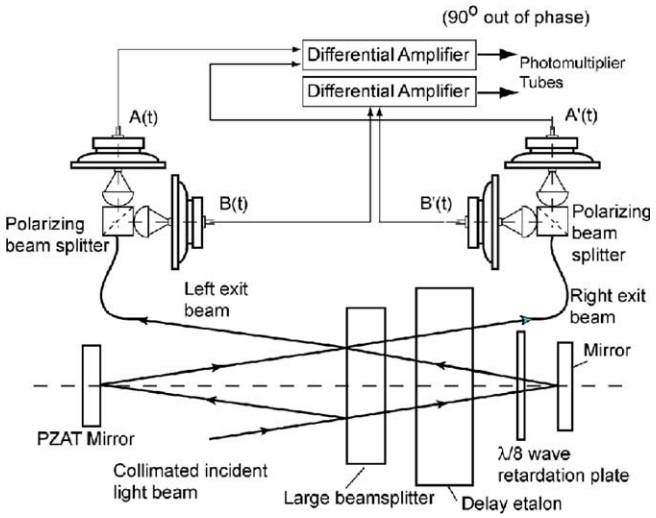


Fig. 12. Schematic showing the light path in a VISAR interferometer.

The schematic of the light path of the laser interferometer is shown in Fig. 12. The VALYN VISAR is based on the wide angle Michelson interferometer (WAMI) concept and capable of velocity measurements from either a spectrally or diffusely reflecting specimen surface. Using a laser light coupler, the light from the laser is coupled into an optical fiber of diameter 125 μm which directs light onto the surface of the specimen. Using an optical assembly called the optical fiber probe, the reflected light is collected and coupled into an out-going fiber which has a diameter of 300 μm. The laser light from the out-going fiber, which contains the Doppler shift effect due to the motion of the surface under shock loading, is collimated and then directed into the VISAR optical system to extract the interferometer information of particle velocity. In order to monitor any intensity change of the reflected laser beam resulting from self illumination due to shock compression, part of the light is sampled by a beam sampler and directed to a photomultiplier tube, which converts the light signal into an electric signal to be recorded on the oscilloscope. The 50/50 large beam splitter evenly splits the light from the main beam into two; one is sent to a PZAT mirror of the interferometer, while the other passes through a 1/8 wave plate, etalon and then is returned by a mirror. One half of the returned light passing through the 50/50 large beam splitter is combined with the reflected part of the returned beam from PZAT mirror to form interference fringes. The other half of the returned light from the PZAT mirror is combined with the beam passing through the 50/50 large beam splitter and reflected from the mirror to form interference fringes. The alignment of the interfering laser beams which give rise to the interference fringe pattern is optimized by monitoring the bull's eyes pattern. Each interference pattern then passes through two separate polarizing beam splitters, separating the $S$ and $P$ components of the laser light, which have a 90° phase angle difference due to the retardation of a 1/8 wave plate to the phase angle of the $P$ component of light. In order to increase the signal to noise ratios the two s-polarized beams and the two p-polarized beams, which are both 180° out of phase, are subtracted (Hemsing, 1979). This feature known as push-pull significantly reduces the noise level introduced by incoherent light entering the interferometer. The subtracted $S$ and $P$ components of the interference fringes are directed into two photomultiplier tubes. Separately recording the $S$ and the $P$ fringes (quadrature coding) eliminates the ambiguity in the sign of the acceleration and improves accuracy when data reduction is performed using the high resolution regimes of the traces. The electrical signals from the photomultipliers are amplified by 1.2 GHz bandwidth amplifies before being sent to 1 GHz digital oscilloscope for recording.

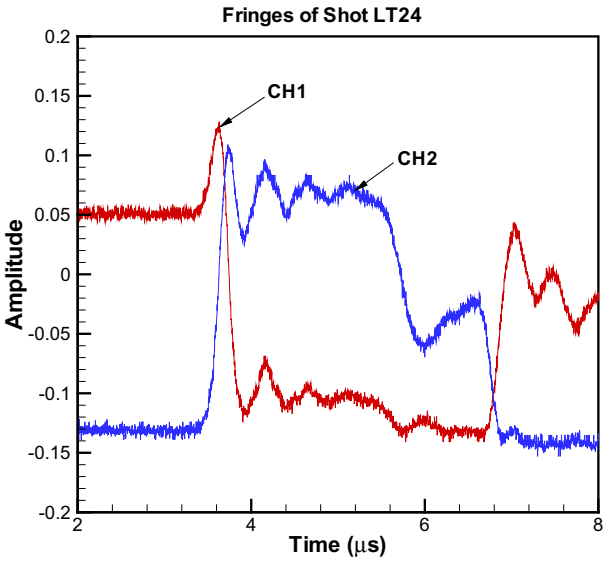


Fig. 13. Oscillographs of VISAR signals for Shot LT24.

Fig. 13 shows a typical oscillograph of the recorded VISAR signal (Shot LT24). The resonant oscillations induced by the multiple reflections of the shock wave at the material interfaces are clearly seen in the record. Part of the data reduction procedure involves plotting the amplitudes of the two fringe records against each other at each data reading time, thereby forming a Lissajous plot of the data. This plot for Shot LT24 is shown in Fig. 14. The Lissajous plot allows the user to judge whether certain corrections to the input data are warranted. The judgement is based in part on how nearly the Lissajous plot resembles a perfect circle, which would be the result if the fringe amplitudes of the two data sets were equal, and if the

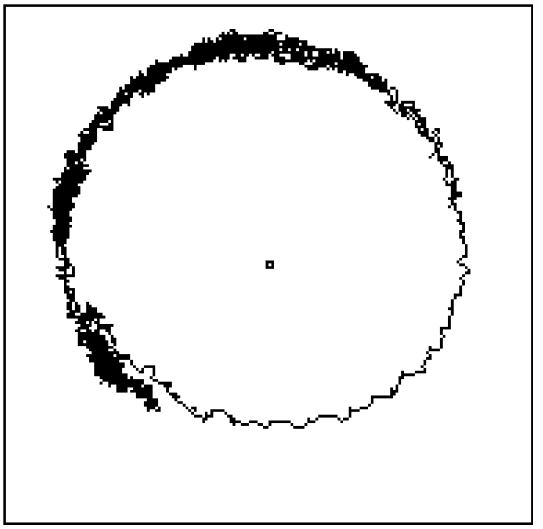

Fig. 14. Lissajous showing the amplitude of the VISAR fringe records plotted against each other at each time data.

phase difference were 90°. Judging from Fig. 14, the Lissajous of this experiment is a near perfect circle, which confirms the high quality of the interference signal.

## 6. Results and discussion

In the present study four series of experiments were designed and conducted. The first series of experiments involved the investigation of the effect of distance of propagation on elastic precursor decay and the late-time dispersion. The experiments were conducted using Fe–Ti laminates. The thickness of each Fe and Ti layer in the laminate was 0.75 mm. A schematic of the experimental configuration is shown in Fig. 15. In the first experiment (Shot LT07) 12 alternating layers of Fe and Ti with a total laminate thickness of 9 mm were utilized. In the second experiment (Shot LT06) four alternating layers of Fe and Ti with a total laminate thickness of 3 mm were utilized. For both experiments the flyer plate was made from hardened CH tool-steel, and was approximately 16 mm in thickness. The thicknesses of the front and rear CH tool-steel plates that sandwich the laminate were 8.65 and 5.14 mm, respectively. The relatively large thickness of the flyer plate precludes any unloading waves from the back surface of the flyer plate to reach the flyer/target interface during the total window time of the experiment.

Fig. 16 shows experimental results on the Ti–Fe laminates. The impact velocities for Shots LT07 and LT06 were 74 and 79 m/s, respectively. In the figure the abscissa represents the time after impact while the ordinate represents the normalized particle velocity measured at the free surface of the target plate. For both experiments the impact velocity is used as the normalization factor for the $y$-axis. The elastic precursor arrives at the free surface of the target plate at approximately 4.2 μs for Shot LT06 and at 5.65 μs for Shot LT07. The later arrival of the elastic precursor in the case of Shot LT07 is consistent with the larger thickness of the laminate employed in Shot LT07. The precursor decay is much higher for Shot LT07 indicating that the decay increases with distance of propagation. The late-time dispersion arrives after the arrival of the elastic precursor. The highest particle-velocity attained observed in the measured wave profiles is approximately 1.2 times the impact velocity and the late-time dispersive wave is observed to oscillate

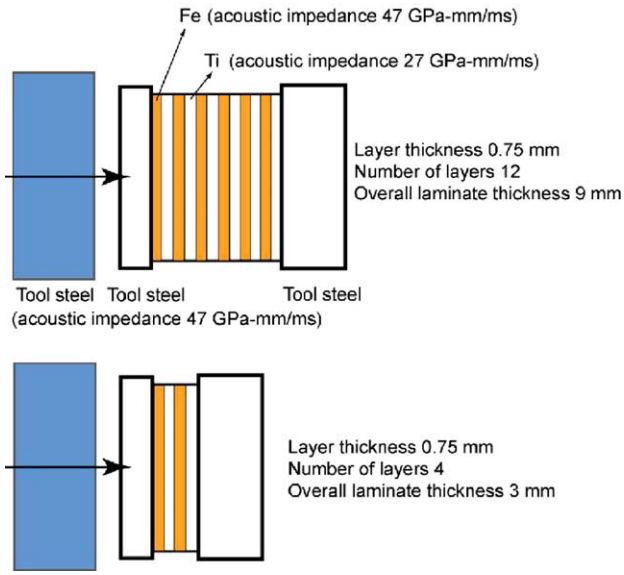


Fig. 15. Schematic of the laminate architecture employed to conduct the first series of plate-impact experiments.

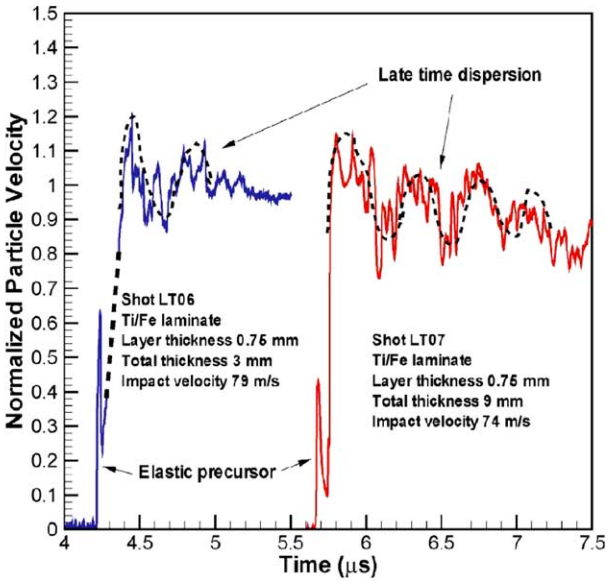


Fig. 16. Results of plate-impact experiments on Fe–Ti laminates showing the effect of distance of propagation on precursor decay and late-time dispersion.

about a mean level 1.0. As expected, the frequency of the oscillations is not affected by the distance the wave propagates into the laminates and is essentially the same for the two experiments. Also, the amplitude of these oscillations is observed to decay with time. It is interesting to note that the general characteristics of the wave structure are strikingly similar to the analytical predictions for wave front and late-time dispersive waves as shown in Fig. 6.

The second series of experiments was conducted to understand the effects of density of interfaces on the elastic precursor decay and late-time dispersion. Again, in this series of experiments Fe–Ti laminates were utilized. A schematic of the layer architectures employed in this series of experiments is shown in Fig. 17. For the two experiments the overall thickness of the laminate was 9 mm. In the first experiment (LT07) 12 alternating layers of Fe and Ti with an individual layer thickness of 0.75 mm were utilized. In the second experiment 6 alternating layers of Fe and Ti with an individual layer thickness of 1.5 mm were utilized. Fig. 18 shows the results of the two experiments conducted in this series. The impact velocities for Shot LT07 and LT09 were 74 and 71 m/s, respectively. It can be seen that the precursor decay for Shot LT07 is much greater than that obtained for Shot LT09. Moreover, the rise-time associated with the late-time dispersive wave is shorter for Shot LT07 when compared with Shot LT09. The frequency of oscillations in the late-time dispersive wave is higher for the Shot LT07 when compared with Shot LT09. These results are all consistent with the analytical results shown in Fig. 8 for Fe–Ti laminates.

The objective of the third series of experiments was to understand the effects of impedance mismatch, density of interfaces, and the material inelasticity on precursor decay and late-time dispersion. These experiments were conducted by employing Al–PC laminates. A schematic of the laminate architectures used in the series of experiments is shown in Fig. 19. For shot LT23 the thickness of the Al and PC layers were 0.75 and 0.8 mm, respectively. The total number of layers was 4 with an overall thickness of 3.1 mm. The laminate was sandwiched between impedance matched 7075-T6 Al front and rear target plates. Moreover, the layers in the laminate were bonded to each other by using a low viscosity epoxy. For shot LT24 the thickness of the Al and PC layers was 0.25 mm. A total of 12 Al and PC layers were used to make the laminate,

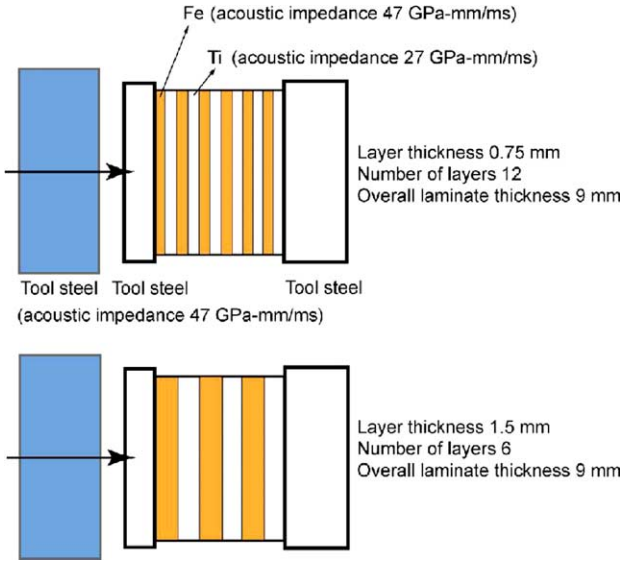


Fig. 17. Schematic of the laminate architecture employed to conduct the second series of plate-impact experiments.

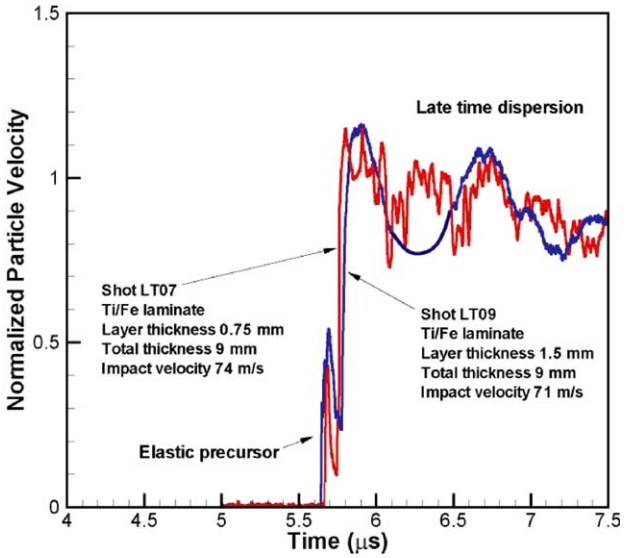


Fig. 18. Results from plate-impact experiments on Ti–Fe laminates, LT07 and LT09, showing the effects of layer thickness on elastic precursor decay and late-time dispersion.

with a total laminate thickness of 3.0 mm. Again, for this experiment the laminate was sandwiched between impedance matched 7075-T6 Al front and rear target plates. Also, the layers in the laminate were bonded to each other with a low viscosity epoxy.

Figs. 20 and 21 show the experimental results obtained from the two experiments on the Al–PC laminates. The impact velocities for Shots LT23 and LT24 were 84 and 82 m/s respectively. For both experiments the flyer plate and the front and rear target plates are made from 7075-T6 Al alloy. The relatively

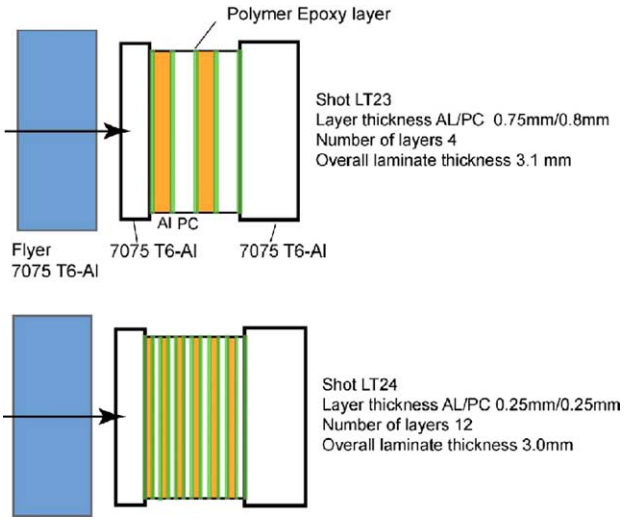


Fig. 19. Schematic of the laminate architecture employed to conduct the third series of plate-impact experiments.

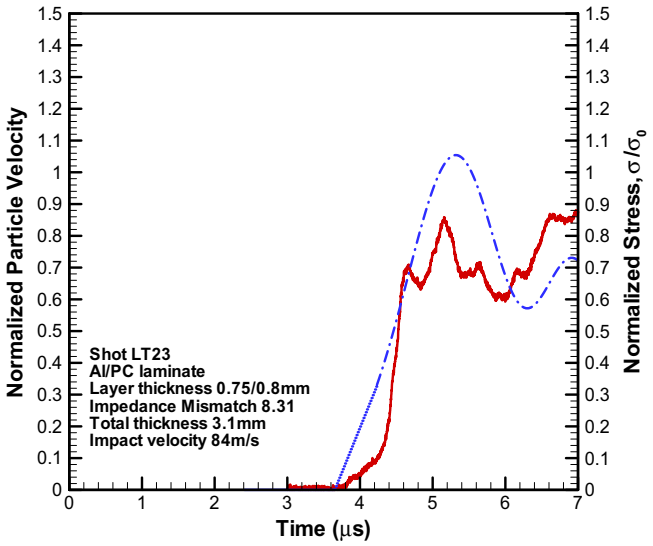


Fig. 20. Results from plate-impact experiments on Al–PC laminates showing the late-time dispersion wave.

large thickness of the flyer plate precludes any unloading waves from the back surface of the flyer plate to reach the flyer–target interface during the window time of the experiment. In both plots the abscissa represents the time after impact while the two ordinates represent the normalized particle velocity measured at the free surface of the target plate and the normalized stress obtained by using Eq. (29), respectively. It is interesting to note that the velocity versus time profiles obtained in the experiments are much smoother when compared with the particle velocity profiles obtained for the elastic–elastic (Fe–Ti) bilaminates. In the case of the Fe–Ti bilaminates a high frequency oscillatory signal was observed to be riding on top of

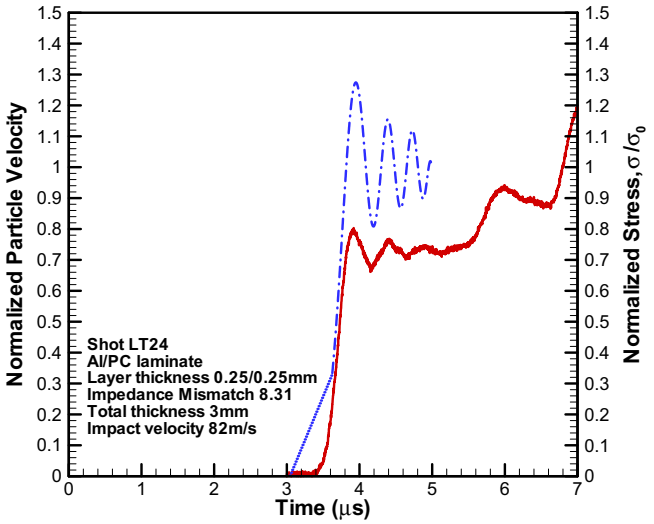


Fig. 21. Results from plate-impact experiments on Al–PC laminates showing the late-time dispersion wave.

the particle-velocity profiles. The presence of air gaps of several microns between the Fe–Ti layers are understood to be the origin of the high frequency oscillations observed in the signal. The reason for the absence of these oscillations in the Al–PC laminates is understood to be due to the use of epoxy in preparing the Al–PC laminates. The use of epoxy to bond the individual layers precludes any air gaps in between the layers. The parameters of the visco-elastic material model for PC that are used in the simulations correspond to nearly elastic behavior, i.e. $\gamma \sim 1$. It is interesting to note that the predicted and the experimentally observed arrival times of the late-time dispersive waves are very close. Also, the frequency of the oscillations contained in the late-time dispersive wave corresponds closely to the analytical predictions with $\gamma \sim 1$ for PC. It should be noted that the experimental results are for particle velocity on the rear surface of the target plate while the analytical solutions are for stress (shown on the $Y_2$-axis).

It is also interesting to compare the experimental results for Shot LT06 and Shot LT23. For Shot LT06 experiments were conducted using Fe–Ti bilaminates with layer thickness of 0.75 mm. The total laminate thickness was 3 mm. For Shot LT23 the laminate comprises Al–PC layers with layer thickness of 0.75 mm and an overall laminate thickness 3 mm. The difference between the two architectures is the impedance mismatch at the layer interface. For the case of Al–PC laminates the impedance mismatch is 8.3, while for the case of the Fe–Ti laminates the impedance mismatch is 1.75. It is interesting to note the relatively long rise-time associated with the late-time dispersive waves for the case of the higher impedance mismatch Al–PC laminates. Also, as predicted by the analytical results, the frequency of the late-time dispersive waves is much smaller for the case of the higher impedance Al–PC laminates as compared with the Fe–Ti laminates.

The fourth series of experiments was conducted to understand wave propagation in elastic–viscoelastic laminates confined by high impedance elastic plates. The high impedance plates result in reverberation of stress waves within the relatively low impedance sandwiched laminate resulting in an incremental build up of stress with each reverberation of stress wave. In this series of experiments Al–PC bilaminates were utilized. The thickness of each Al and PC layer is 0.125 mm. In the first experiment the laminate comprised four alternating layers of Al and PC with a total laminate thickness of 0.5 mm. For the second experiment eight alternating layers of Al and PC with a total laminate thickness of 1.0 mm were utilized. For the third experiment 12 alternating layers of Al and PC with a total laminate thickness of 1.5 mm were utilized. In each case the Al–PC laminate was sandwiched by high impedance steel plates. A

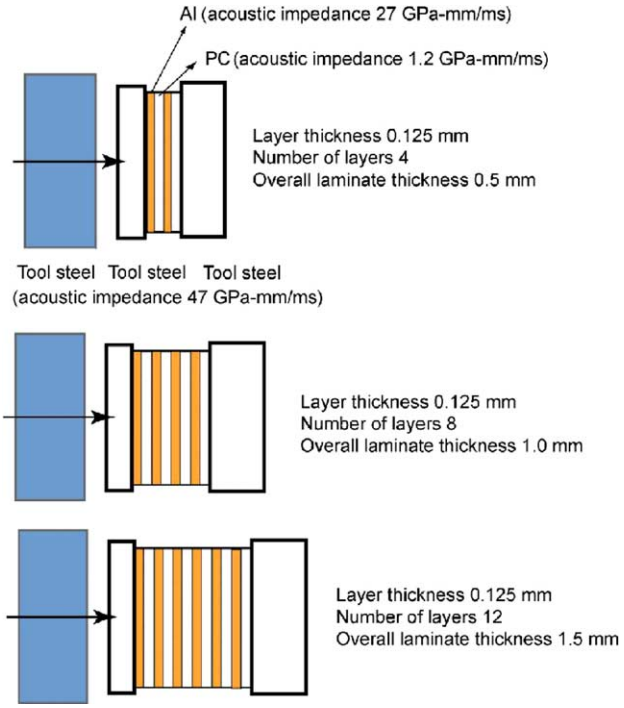


Fig. 22. Schematic of the laminate architecture employed to conduct the fourth series of plate-impact experiments.

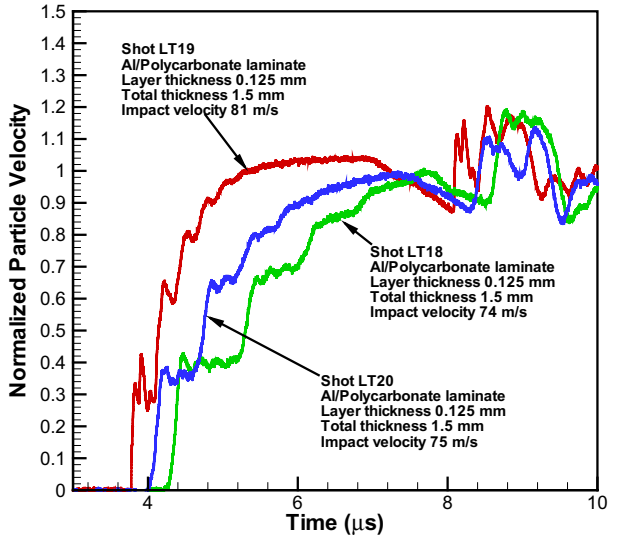


Fig. 23. Results from plate-impact experiments on thin Al–PC laminates sandwiched between two hard CH tool-steel plates.

schematic of the experimental configurations for this series of experiments is shown in Fig. 22. Fig. 23 shows experimental results on the Al–PC laminates. The impact velocities for the three experiments,

LT19, LT18, and LT20 were 81, 74 and 75 m/s, respectively. The abscissa shows the time after impact while the ordinate shows the normalized particle velocity. It is seen that in each case, the normalized particle velocity (or the stress) builds up to the impact velocity in a series of steps. Each step represents one reverberation of the stress wave between the CH steel plates. As expected the time duration of each step is longest for the laminate with the greatest thickness, i.e. Shot LT18 with 12 alternating layers of PC and Al. Also, it is interesting to note the oscillatory nature of the particle velocity profile at each loading step. The sudden increase in particle velocity at approximately 8 μs is consistent with the arrival of the release wave from the lateral boundary. Full simulations of the experiments utilizing finite element methods are required to adequately model the observed velocity versus time profiles for the three sandwiched laminates.

## 7. Summary

In the present study normal plate-impact experiments are conducted on 2-D layered material targets to understand the role of material architecture and material inelasticity in governing the elastic precursor decay and late-time wave dispersion. The particle velocity at the free surface of the target plate is measured by using a multi-beam VALYN VISAR. In order to understand the effects of layer thickness and the distance of wave propagation on elastic precursor decay and late-time dispersion several different targets with various layer and target thicknesses are employed. Moreover, in order to understand the effects of material inelasticity both elastic–elastic and elastic–viscoelastic bilaminates are utilized.

The results of these experiments are interpreted by using asymptotic techniques to analyze propagation of acceleration waves in 2-D layered material systems. The analysis makes use of the Laplace transform and Floquet theory for ODE's with periodic coefficients (Chen and Clifton, 1974). Both wave-front and late-time solutions for step-pulse loading on layered half-space are compared with the experimental observations.

The results of the study indicate that the structure of acceleration waves is strongly influenced by impedance mismatch of the layers constituting the laminates, density of interfaces, distance of wave propagation, and the material inelasticity. The speed of the elastic precursor is independent of the impedance mismatch of the individual laminae constituting the bilaminates and is equal to the average wave speed within the bilaminates. The speed of late-time dispersion wave is observed to decrease with an increase in impedance mismatch; however, it is found to be independent of the density of interfaces, i.e. the number of layers in a given thickness laminate. The decay in elastic precursor is observed to increase with an increase in impedance mismatch, the density of interfaces, and the distance of wave propagation. The rise-time of the late-time dispersion wave increases with an increase in impedance mismatch; however, it is observed to decrease with an increase in the density of interfaces. The frequency of oscillations of the late-time dispersive wave is observed to decrease with an increase in impedance mismatch; however, it is observed to increase with an increase in the density of interfaces.

## Acknowledgments

The authors would like to acknowledge the DoD Army General, Army Research Office, for financial support for this research work under contract no. DAAD19-01-1-0782, Program Director: Dr. David Stepp. The authors would also like to acknowledge Dr. A. Rajendran of the Army Research Office for his interest and several enlightening discussions on the subject. The authors would also like to acknowledge the financial support from the National Science Foundation through grant CMS-0079458 for the acquisition of the multi-beam VALYN VISAR system used in the present experiments.

## References

Achenbach, J.D., 1973. Wave Propagation in Elastic Solids. North-Holland, Amsterdam.

Barker, L.M., Lundergan, C.D., Chen, P.J., Gurtin, M.E., 1974. Nonlinear viscoelasticity and the evolution of stress waves in laminated composites: a comparison of theory and experiment. Journal of Applied Mechanics 41, 1025.

Benson, D.J., Nesterenko, V.F., 2001. Anomalous Decay of shock impulses in laminated composites. Journal of Applied Physics 89 (7), 3622–3626.

Betheney, W., DeLuca, E., Prifti, J., Chou, S.C., 1998. Ballistic impact damage of S2-glass reinforced plastic structural armor. Composites Science and Technology 58, 1453–1461.

Cerrillo, M.V., 1950. Technical Report No. 55, 2a, Research Laboratory of Electronics MIT, Cambridge, MA.

Chen, C.C., Clifton, R.J., 1974. Asymptotic solutions for wave propagation in elastic and viscoelastic bilaminates. In: Developments in Mechanics, Proceedings of the 14th Mid-Eastern Mechanics Conference, vol. 26, no. 8, pp. 399–417.

Clifton, R.J., 1972. Solution of wave problems in inelastic materials. In: Summer Course on Dynamics of Inelastic Materials. Jablonna, Poland.

Fink, B., 2000. Performance metrics for composite integral armor. Journal of Thermoplastic Composite Materials 13 (5), 417–431.

Hegemier, G.A., 1972. On a theory of interacting continua for wave propagation in composites. In: Lee, E.H. (Ed.), Dynamics of Composite Materials. ASME, pp. 70–121.

Hemsing, W.F., 1979. Velocity sensing interferometer (VISAR) modification. Review of Scientific Instrumentation 50 (1), 73–78.

Laptev, V.I., Trishin, Y.A., 1976. The increase of velocity and pressure under impact on inhomogeneous target. Journal of Applied Mechanics and Technical Physics, 837–841.

Lundergan, C.D., Drumheller, D.S., 1971. Dispersion of shock waves in composite materials. Shock Waves and the Mechanical Properties of Solids. Syracuse University Press, New York, . 141.

Nesterenko, V.F, Fomin, V.M., Cheskidov, P.A., 1983. Attenuation of strong shock waves in laminate materials. Nonlinear Deformation Waves. Springer-Verlag, Berlin, p. 191–197.

Nesterenko, V.F., Fomin, V.M., Cheskidov, P.A., 1984. Damping of strong waves in laminar materials. Journal of Applied Mechanics and Technical Physics, 567–575.

Oved, Y., Luttwak, G.E., Rosenberg, Z., 1978. Shock wave propagation in layered composites. Journal of Composite Materials 12, 84.

Peck, J.C., Gurtman, G.A., 1969. Dispersive pulse propagation parallel to the interfaces of a laminated composite. Journal of Applied Mechanics, 479–484.

Sherby, O.D., Lee, S., Koch, R., Sumi, T., Wolfenstine, J., 1990. Multilayered composites based on ultrahigh carbon steel and brass. Materials and Manufacturing Processes 5, 363–376.

Stern, M., Bedford, A., Yew, C.H., 1970. Wave propagation in viscoelstic laminates. Journal of Applied Mechanics 70-WA/APM-40, 1–7.

Sun, C.-T., Achenbach, J.D., Herrmann, G., 1968. Time-harmonic waves in a stratified medium propagating in the direction of the layering. Journal of Applied Mechanics, 408–411.

Sve, C., 1971. Thermo-elastic waves in a periodically laminated medium. International Journal of Solids Structures 7, 1363–1373.

Sve, C., 1972. Stress wave attenuation in composite materials. Journal of Applied Mechanics, 1151–1153.

Vaidya, U.K., Hosur, M.V., Kumar, P., Mahfuz, H., Haque, A., Jeelani, S., 1999. Impact damage resistance of innovative functional sandwich composites. In: ASME 1999 Mechanics and Materials Conference Blacksburg, VA.

Zhuang, S., 2002. Shock wave propagation in periodically layered composites. Ph.D. Dissertation. California Institute of Technology, Pasadena, CA.